RSC Pharmaceutics

ROYAL SOCIETY OF CHEMISTRY

PAPER

View Article Online
View Journal | View Issue

Cite this: *RSC Pharm.*, 2024, **1**, 806

Dual-purpose resveratrol-quantum dots loaded albumin nanoparticles†

Deepankar Yadav,[a] Priyanka Chaudhary,[b] Priya Singh,[a,c] Monu Gupta[b] and Shubhini A. Saraf *[a,d]

Received 1st April 2024,
Accepted 10th August 2024

DOI: 10.1039/d4pm00100a

rsc.li/RSCPharma

Incorporating therapeutic and imaging capabilities into core–shell structured nanoparticles (NPs) has shown promising results in cancer treatment. This study aims to develop paddy husk carbon quantum dots (QDs) encapsulated in bovine serum albumin (BSA) nanoparticles with resveratrol (RSV) to enhance antioxidant activity and bioimaging potential. Carbon QDs, approximately 10 nm in size, were synthesized and characterized by UV-visible spectroscopy, photoluminescence spectroscopy, TEM, and FTIR. The optimized formulation was achieved using a full-factorial design, resulting in a combination of BSA with concentration of 219.004 mg, RSV with concentration of 8.271 mg, and 4 mL of ethanol. The nanoparticles exhibited a particle size of 125.6 nm, a zeta potential of −0.570 mV, 63.06% entrapment efficiency, and 7.173 mg drug content. *In vitro* assays showed that the nanoparticles enhanced RSV release under mildly acidic conditions, demonstrating efficacy as intracellular drug carriers. Cytotoxicity assays against MDA-MB-231 cells revealed dose- and time-dependent cytotoxicity, with 72% cell viability for the optimized formulation at the highest concentration tested. Antioxidant activity was 96% for the optimized formulation, compared to 35–45% for QDs and 80–85% for RSV alone, as measured by DPPH and H_2O_2 assays. Confocal microscopy confirmed the superior imaging capability of the QDs. These findings indicate that QD- and resveratrol-loaded albumin nanoparticles (ANPs) have the potential to serve as effective cancer therapeutic agents and as biological imaging probes.

1. Introduction

Carbon quantum dots (QDs) are new nanostructures with specific properties; their bandgap varies with size and they exhibit photoluminescence. Less than ten nanometer-sized carbon nanoparticles, known as carbon quantum dots (QDs), can produce different colors because of confinement and size effects.[1,2] In semiconductor materials, charge carriers have various energy levels, which are close to each other, forming energy bands. When the size of the crystal becomes similar to the Bohr radius, the electron energy levels separate.[3] In developing photovoltaic devices, photocatalysis, chemical sensing, biosensing, bioimaging for intracellular targeting, and in many more fields, great use for carbon quantum dots has been found.[4]

Reactive oxygen species (ROS) injure proteins or carbohydrates, producing oxidative stress because of the oxidation of metabolic by-products, causing cell death or necrosis. Antioxidants can lessen or prevent harm like oxidative degradation from high amounts of free radicals.[5] Consequently, various industries, such as food and beverage, packaging, cosmetics, and health, depend on antioxidants and free-radical scavengers for reducing oxidative degradation. Carotenoids and other chemicals with lengthy conjugated carbon chains are often suitable as free-radical scavengers. Research has been performed on various carbon nanomaterials as scavengers of ROS and free radicals.[6]

Carbon quantum dots appear to have little cytotoxicity and good biocompatibility,[7] meeting the fundamental requirements for *in vivo* imaging of cells and tissues. Paddy husk is a promising material for carbon quantum dots (PCQDs), with excellent water solubility, low toxicity, and good free-radical scavenging action. The C-dots (N/S-CDs) prepared from

[a]*Department of Pharmaceutical Sciences, Babasaheb Bhimrao Ambedkar University, Lucknow, 226025, India*
[b]*Nanomaterials and Sensors Research Laboratory, Department of Physics, Babasaheb Bhimrao Ambedkar University, Lucknow-226025, India*
[c]*School of Pharmacy, GITAM (Deemed-to-be) University, Rudraram, Patancheru Mandal, Hyderabad-502329, Telangana, India*
[d]*National Institute of Pharmaceutical Education and Research, Bijnor-Sisendi Road, Sarojini Nagar, Near CRPF Base Camp, Lucknow (UP)- 226002, India.*
E-mail: shubhini.saraf@gmail.com

† Electronic supplementary information (ESI) available. See DOI: https://doi.org/10.1039/d4pm00100a

cellulose-based bio-waste show high fluorescence quantum yields. These PCQDs can neutralize free radicals and suppress lipid peroxidation, reducing the risk of oxidative stress-related illnesses and cell damage.[8]

Several green methods for synthesizing QDs using natural products like red cabbage, rice husk, and bio-waste have been reported.[9] Bacterial species absorb the synthesized QDs, revealing their low levels of cytotoxicity and potential for bio-imaging applications.[10] Various carbon nanodots (CNDs) have been produced by hydrothermally processing *Mahonia oiwakensis* Hayata (MO) plant parts and other agricultural waste. The CNDs were made by carbonizing various types of bamboo and wood.[11] Graphene quantum dots have also been synthesized on a large scale from rice husk biomass.[12]

Here, we have synthesized carbon quantum dots using paddy husk (PCQDs), the protective covering of rice grains. Paddy husk is a by-product of rice milling and is typically considered agricultural waste. It has been employed as a raw material for synthesizing QDs since it is plentiful and inexpensive.[13–17]

PCQDs have high quantum yield, intense blue fluorescence, and are stable in water. In this work, we prepared carbon quantum dots from an environmentally friendly, agri-waste material, paddy husk. First, we assessed the cytotoxicity and antioxidant properties and obtained favorable results. Furthermore, the 2,2-diphenyl-1-picrylhydrazyl (DPPH) assay is a well-known, rapid, simple, and reasonably priced way to measure antioxidant activity. It uses free radicals to evaluate the capacity of a substance as a hydrogen supplier or free-radical scavenger (FRS). The separation of fluorescent carbon dots with quantifiable antioxidant properties from paddy husk, an agricultural waste source, makes this study novel.

Carbon quantum dots have acquired massive recognition among scientists due to their abundance, ecofriendly nature, water solubility, assorted usefulness, and biocompatibility when contrasted with other traditional quantum dots.[18,19] Carbon dots are quasi-spherical nanoparticles that can be synthesized by various strategies.[20] The bottom-up technique uses small organic atoms joined by microwave, thermal pyrolysis, and aqueous or solvothermal decomposition through partial dehydration and dehydrogenation.[21] However, the top-down strategy continues to break down somewhat larger particles into smaller particles or nanoparticles through laser techniques.[22] In general, quantum dots consist of a metallic core that can emit fluorescence, surrounded by a covering substance that prevents photobleaching and spilling. The central material is selected based on the ratio of light emitted to light absorbed by fluorophores to produce the most extreme quantum yield, which indicates the luminescence of the fluorescent material.[23] Each energized electron is anticipated to reach the ground state and connect with its hole to create fluorescence. Carbon quantum dots have numerous chemical and mechanical properties, like enhanced fluorescence, high photostability, and excellent biocompatibility. Carbon dots are helpful nanotechnology instruments for the diagnosis and treatment of cancer.[24] Natural carbon dots are used in drug delivery for sensing and tracing probes, photo-activated antimicrobial activity, cell reinforcement, and as neurodegenerative agents.[25] They can be designed to attach valuable functional groups, such as amine, carboxyl, carbonyl, hydroxyl, ether, epoxy, and heteroatoms. Such surface functional groups greatly influence the characteristics of carbon dots. Surface functionalization enhances solubility in fluid arrangements as well as non-aqueous arrangements, while surface passivation improves fluorescence.[26] Oxidative degradation caused by increased free radicals is one type of harm that antioxidants can prevent or minimize. Reactive oxygen species can be eliminated or reduced by antioxidants to a suitable level, preserving the normal function of biological systems.[27] Research on the antioxidant activity of carbon quantum dots and their related antioxidant pathways is still significant and valuable for treating diseases, particularly those generated by free radicals directly or indirectly.[28]

Resveratrol is a powerful antioxidant with good bioactivity.[24] However, it holds certain limitations, such as low solubility (30 mg L^{-1}), short half-life (<1 h), and short circulation time. Delivering resveratrol *via* a suitable nanocarrier may help overcome these drawbacks. This research work envisaged synergizing the activity of resveratrol with quantum dots to enhance antioxidant activity, increase circulation time, circumvent RES uptake as the particle may become bigger, and improve its half-life using a suitable nanocarrier. The current efforts aim to overcome toxicity by creating quantum dots from natural sources, imaging cancer cells using biosensing techniques, and boosting antioxidant qualities using an appropriate nanocarrier system. To our knowledge, no work has been reported on quantum dots using paddy husk.

2. Material and methods

2.1. Materials

Paddy husks were collected from a paddy mill at Hardatt Nagar Girant village, District of Shravasti, Uttar Pradesh. They were used as a precursor for synthesizing carbon quantum dots (carbon source). Methyl thiazolyl tetrazolium (MTT), DPPH, and hydrogen peroxide were purchased from Thermo Fisher Scientific Pvt. Ltd, Mumbai, India. Mouse skin fibroblast (MDA-MB-231) and L929 cells were obtained from the National Centre for Cell Sciences (NCCS) in Pune, Maharashtra, India. Cayman Chemical Company (E. Ellsworth Road, Ann Arbor, MI, USA) supplied the RSV.

2.2. Preparation of carbon quantum dots

The detailed synthesis method of PCQDs (from paddy husk) is shown in Fig. 1. The required paddy husk was collected and carbonized at 350 °C for 4 h in a digital furnace. The carbonized husk particles were finely ground by subjecting them to shear forces in a mortar to reduce the particle size further. The resultant fine powder (0.1 g) was dissolved in 10 mL of DW under stirring for 8 h to prepare a solution. After passing

Fig. 1 Synthesis of carbon quantum dots through a green route.

through 0.22 μm pore filter paper, the solution was kept at ambient temperature for further analysis.[29]

2.3. Preparation of albumin nanoparticles

The desolvation procedure was used to prepare BSA (bovine serum albumin) nanoparticles with slight modification by utilizing 4 mL of water to dissolve 250 mg of BSA powder. Subsequently, 8 mL of ethanol was added dropwise at 2 mL min^{-1} to the BSA solution with constant stirring (1250 rpm) at room temperature using specially built apparatus. The presence of translucency in the fluid suggested that the nanoparticles were formed. To stabilize the unstable particles through cross-linking, 1-ethyl-3-(3-dimethyl aminopropyl) carbodiimide hydrochloride (EDC) (5 mg in 0.5 mL water) was added (Fig. 2). The stirring condition was maintained for three hours to ensure all amino acid residues were cross-linked.[30]

2.4. Co-loading of RSV and QDs in albumin NPs

The desolvation process was used to co-load resveratrol and QDs into albumin nanoparticles. BSA was weighed and mixed with carbon quantum dot-infused distilled water. Subsequently, using the specific apparatus and under continuous stirring (1250 rpm with a 1 cm magnet), ethanol was added dropwise at 2 mL min^{-1} to the BSA mixture at room temperature. The presence of turbidity in the fluid suggested that the nanoparticles were forming. To stabilize the unstable particles through cross-linking, 1-ethyl-3-(3-dimethyl-aminopropyl) carbodiimide hydrochloride (EDC) (5 mg in 0.5 mL water) was added. The solution was continuously stirred for three hours to ensure all amino acid residues were cross-linked.

2.5. Instrumentation and characterization

2.5.1 Particle size, PDI and zeta-potential. The particle size and PDI of albumin nanoparticles were analyzed according to reports in the literature.[31] A Nano Plus zeta/nanoparticle analyzer was used to examine the particle size and PDI of the albumin nanoparticles. Before these determinations, the sample was prepared in triplicate by dispersing albumin nanoparticle-loaded resveratrol and quantum dots in distilled water. One method for figuring out the surface charge of a nanoparticle is zeta potential analysis. The zeta potential of the albumin nanoparticle-loaded resveratrol and quantum dots was measured using a Malvern Nanosizer ZS instrument (Malvern Instruments, UK) at 25 °C.

2.5.2 Morphological evaluations. A scanning electron microscopy (SEM) specimen was mounted on a metal stub and visualized *via* an SEM model JSM6490 under low vacuum at the University Sophisticated Instrumentation Center (USIC), BBAU, Lucknow.

2.5.3 Transmission electron microscopy. Transmission electron microscopy (TEM) was carried out according to protocol.[32] It was utilized to examine the internal structure of the nanoparticles. We have utilized high-resolution transmission electron microscopy to observe the internal structure of nanoparticles (FEI Tecnai Spirit, using a 20 kV accelerating voltage).

2.5.4 FTIR analysis. Fourier transform infrared (FTIR) spectroscopy (FT-IR Nicolet, USA6700) was used to record sample spectra. The FTIR analysis aimed to examine the inter-

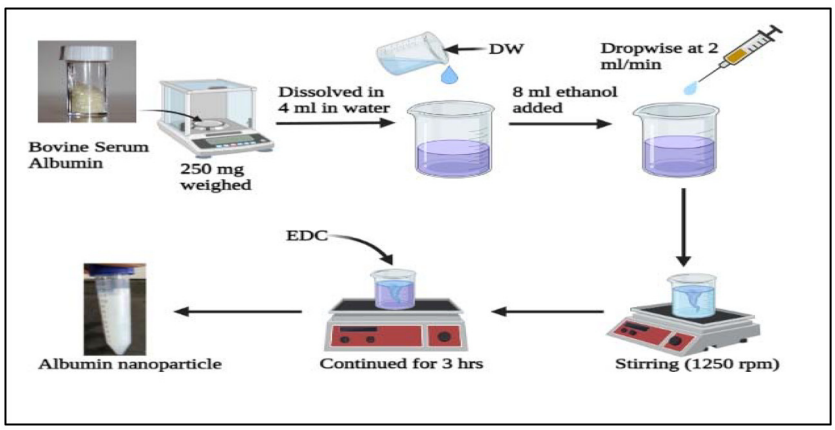

Fig. 2 Preparation of albumin nanoparticles.

molecular interactions between the constituents of resveratrol and quantum dot-loaded albumin nanoparticles. For the FTIR study, the optimized formulation was lyophilized, finely crushed, combined with potassium bromide (1 : 10 ratio by weight), and compressed at 15 000 PSIG to create pellet discs. The pellets were then scanned with the FT-IR Nicolet, USA6700 apparatus, and the spectra were recorded and interpreted.[32]

2.5.5 Entrapment efficiency. To measure the entrapment efficiency, we used an indirect method: we collected the supernatant of a centrifuged sample of nanoparticles and determined the quantity of free drug in it. To isolate the free drug in the supernatant, the formulation was centrifuged at 4500 rpm for 10 min while kept at 4 °C using a high-speed ultracentrifuge. With a UV spectrophotometer set to 302.4 nm, the amount of medication recovered was measured after the supernatant was diluted. The % entrapment efficiency (EE) was calculated using eqn (1):

$$\%\mathrm{EE} = \frac{\text{Weight of intial drug} - \text{weight of free drug}}{\text{Weight of initial drug}} \times 100 \quad (1)$$

2.5.6 *In vitro* drug release. The *in vitro* release of albumin nanoparticles was determined in phosphate buffer (pH 7.4) and acetate buffer (pH 5).[33] The dialysis bag method (12 kDa) was used. First, we washed the dialysis membrane under running water for three to four hours to activate it. It had a one-meter treatment at 80 °C with 0.3% sodium sulfide. After that, the material was acidified for one minute using 0.2% w/v sulfuric acid; it was washed for 2 min at 60 °C and rinsed with hot water. It was then refrigerated and kept in distilled water. The formulation containing 1 mg mL^{-1} was placed in an open-end dialysis tube suspended in 30 mL of pH 7.4 phosphate buffer solution at 37 ± 1 °C and stirred at 120 rpm to measure the cumulative drug release. Samples of 2 mL were removed at prearranged intervals and replaced with the same volume of fresh medium. The samples were examined at 302.4 nm using a UV spectrophotometer. The data are presented as mean ± standard deviation, and the samples were analyzed in triplicate.

2.5.7 Release kinetics study. To assess the drug release mechanism and kinetics, the drug release data of the formulations (albumin nanoparticles) in the current study were plotted using a variety of kinetics models, including zero-order, first-order, Higuchi's kinetics, and Korsmeyer's equation.[33,34] Plots of the gathered data from *in vitro* drug release tests were made using Higuchi's model, which includes the cumulative percentage of drug release *vs.* the square root of time, log of the cumulative percentage of drug remaining *vs.* time, and the cumulative amount of drug release *vs.* time (zero-order).

2.5.8 Antioxidant assays. Two methods were used to detect the antioxidant activity of nanoparticles.

DPPH assay. Various concentrations of the test samples were prepared. An accurately measured quantity of the test sample was transferred to a clean sample tube wrapped in aluminum foil. To this solution, 800 µL of 0.1 M Tris-HCl buffer (pH 7.4) and 1 mL of DPPH solution were added. The resultant solution was mixed well and placed in a dark chamber for 30 min. After analyzing the absorbance at 517 nm, the inhibition ratio was computed using eqn (2):

$$\text{Inhibition ratio}\,(\%) = \frac{\text{Control absorbance} - \text{sample absorbance}}{\text{Control absorbance}} \times 100 \quad (2)$$

H_2O_2 assay. This was performed to determine the CQD free-radical scavenging activity. Various concentrations of test samples were prepared. A phosphate buffer was prepared (as per IP) at pH 7.4. One mL of hydrogen peroxide solution was measured precisely, and 0.6 mL of phosphate buffer (pH 7.4) was added. The test solution was then added immediately. This was left at room temperature for 10 min in a dark chamber. Using a UV-visible spectrophotometer (Labtronics-LT 2910, India), absorbance was measured at 230 nm.[35] The percentage of radical scavenging activity was determined using eqn (3):

$$\%\,\text{Radical scavenging activity} = \frac{\text{Control O.D.} - \text{sample O.D.}}{\text{Control O.D.}} \times 100 \quad (3)$$

2.5.9 *In vitro* cytotoxicity studies. The cytotoxicity of the samples (RSV, QDs, and optimized albumin nanoparticles) was evaluated using an MTT assay. Briefly, MDA-MB-231 cells were cultivated in 96-well plates at a density of 1×10^4 cells per well using a growth medium that included 10% fetal bovine serum and 1% antibiotic-antimycotic solution. The cells were kept at 37 °C in a humidified 5% CO_2 environment for a whole day. Each well was supplemented with a new medium containing varying amounts of optimized albumin nanoparticles, QDs, and RSV and then incubated for 48 hours. After a thorough PBS wash, 20 mL of MTT solution at a concentration of 5 mg mL^{-1} was added to the cells, and they were incubated for an additional 4 h at 37 °C. The MTT solution was then removed, and 100 µL of DMSO was added to each well to dissolve the formed formazan crystals. After shaking the plates for ten minutes, the formed formazan product absorbance at 570 nm was measured. The cytotoxicity was determined by measuring the absorbance of control cells treated with an identical volume of liposomal dispersion media (0.9% w/v of sodium chloride).[36] The formula provided in eqn (4) was used to determine the percentage of cytotoxicity:

$$\%\,\text{Cytotoxicity} = 1 - \left(\text{Optical density(absorbance) of sample/optical density (absorbance) of control}\right) \times 100 \quad (4)$$

2.5.10 *In vitro* cell imaging. MDA-MB-231 cells were grown in HG-DMEM supplemented with 10% FBS, 100 units per mL of streptomycin, and 100 µg mL^{-1} penicillin at 37 °C in 5% CO_2. The BT-549 cells were cultivated in an RMPI-1640 supplement containing 5 mg of bovine insulin, 10% FBS, and 110 mg L^{-1} of sodium pyruvate. After reaching the stationary

phase, the cells were trypsinized and planted at a starting cell density of 1×10^5cells per well in ∅ 30 mm cell culture dishes. The cells underwent three rounds of washing with fresh media before being photographed using a laser-based point-scanning FV1000 confocal fluorescence microscope from Olympus (Japan).[37,38]

2.5.11 Statistical and data assessment. The results were represented as mean average ± SD. The statistical assessment analysis of variance and the Bonferroni test were performed using GraphPad Prism software. A *p*-value less than 0.05 indicated statistical significance.

3. Results and discussion

3.1. Characterization of quantum dots

The interaction between the drug and quantum dot-loaded nanoparticles was confirmed by the FTIR study, as shown in Fig. 3a. The data for carbon quantum dots were observed from a wavelength of 4000 cm^{-1} to 750 cm^{-1}. The corresponding functional groups were subsequently ascertained by interpreting the spectrum's significant peaks. A peak at around 1637.69 cm^{-1} was found to be due to the alkene (C=C) group. Another broad and intense peak for the hydroxyl group was observed at 3308.94 cm^{-1}. These peaks confirmed the functional groups and the purity of the synthesized carbon quantum dots. Photoluminescence spectra of PCQDs are presented in Fig. 3b, which shows the prominent characteristics of the formation of quantum dots. The optical emission spectrum demonstrates the size-dependent features and the distinctive symbol of quantum confinement.[39] With the excitation wavelength at 437 nm, the PCQDs show maximum spectra. The aqueous solution showed a green color in the UV light chamber. The formation of carbon quantum dots was physically confirmed by illumination under UV radiation. The absorption and emission peaks observed through PL indicated that the carbon quantum dots were uniformly formed. It is possible to learn more about the energy transfer procedures inside the material by looking at the photoluminescence spectra for various excitation wavelengths. Multiple emission peaks or variations in peak strength with excitation wavelength might point to flaws in the material or energy transfer between different electronic states. For example, the most significant peak intensity occurs at an excitation wavelength of 437 nm. Photoluminescence spectra can show whether a material has flaws or impurities. These flaws may bring energy levels into the material's bandgap, producing recognizable emission peaks in the ranges. Researchers can learn more about the kind and concentration of flaws or impurities by examining variations in emission intensity and peak locations at various

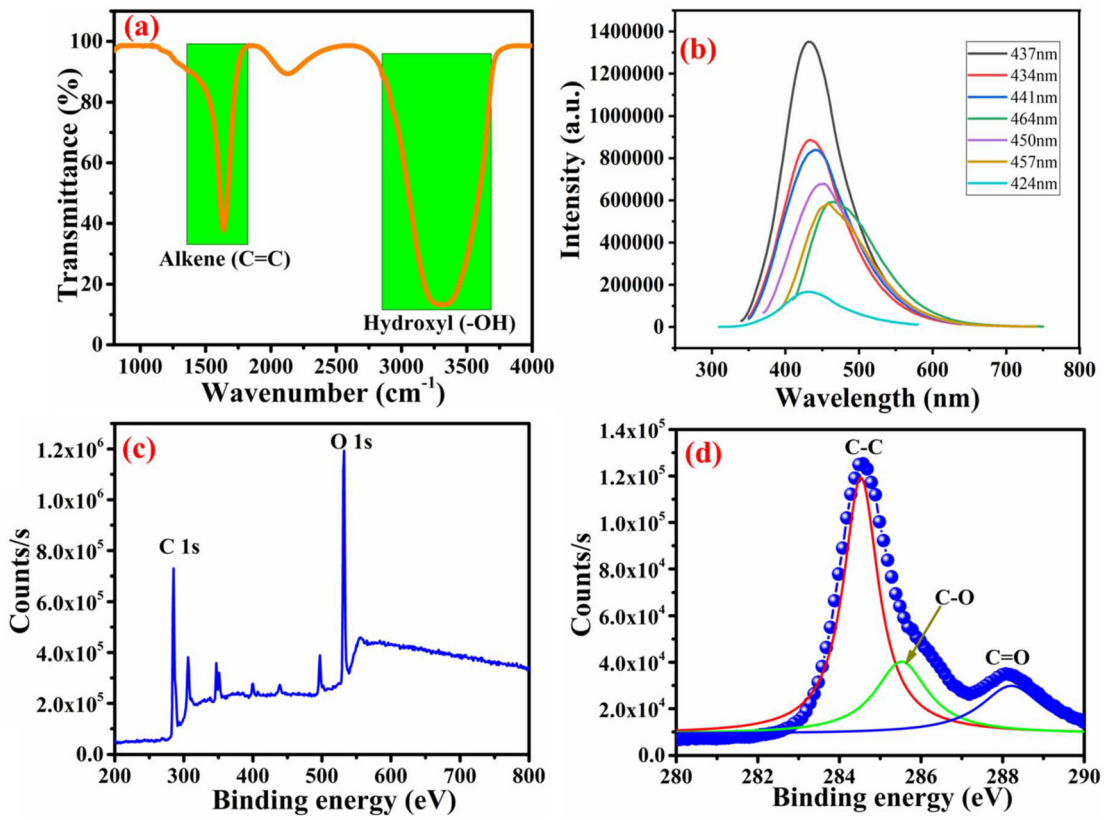

Fig. 3 (a) FTIR of CQDs confirms the functional groups and purity of the synthesized carbon quantum dots. (b) PL spectrum shows that the carbon quantum dots are uniformly distributed. (c) XPS survey spectrum of CQDs and (d) XPS reveals no contaminants and confirms the purity of the PCQDs.

excitation wavelengths. As the excitation wavelength decreases, blue-shifted emission may be seen in the photoluminescence spectra of CQDs. Smaller CQDs have a wider bandgap and emit light at higher energies, which is related to size-dependent quantum confinement effects and the blueshift. Fig. 3c and d show the elemental analysis of PCQDs. The XPS spectrum of the synthesized PCQDs reveals the presence of carbon and oxygen verifying quantum dots. Binding energy positions at 285.8, 285, and 287 eV in the XPS spectrum correspond to deconvoluted peaks that indicate available bonds between C–C, C–O, and C=O.[40] The sharp peak at 285.8 eV shows the sp^2 graphitic structure of synthesized PCQDs. The XPS analysis revealed no contaminants, confirming the purity of the PCQDs in their as-synthesized form.

UV-visible spectroscopy is based on Beer-Lambert's law. A monochromatic light beam is split into two beams of equal intensity when passed through a beam splitter. One of the two beams passes through the material sample, and the other passes through a reference cell. The beams transmitted through the sample and reference cells are measured as I and I_o, respectively.

$$\alpha h\nu = K(h\nu - E_g)^n \quad (5)$$

$$(\alpha h\nu)^{1/n} = A(h\nu - E_g) \quad (6)$$

The direct allowed and indirect allowed bandgaps can be determined by substituting the values of n as 1/2 and 2, respectively. The bandgap of the nanomaterial in PCQDs was determined from eqn (5) and (6) by extrapolating between the $(\alpha h\nu)^{1/2}$ on the Y-axis and hν on the X-axis, as shown in Fig. 4b. The optical bandgap for PCQDs was 5.27 eV, which is too high and confirms quantum confinement.

TEM images, shown in Fig. 4a and b, clearly reveal the particle size distribution of PCQDs. The homogeneous size distribution of the particles is visible in these TEM images. The particle size was determined to be between 2 and 5 nm. The PCQDs are scattered evenly, and there is no prominent grouping. This outcome demonstrated that the PCQDs are made entirely of carbon and not a blend of different organic components.

The particle size distribution was determined using a Nanozetasizer (NSZ90 Malvern) to execute the dynamic light scattering (DLS) method to confirm the size of the carbon quantum dots. Here, the DLS system employs the idea of Brownian motion of particles in a diluted solution of the precursor. When the corresponding data were studied, it was evident that there was just one peak, and the particles were distributed evenly. The average particle sizes were found to be in the range of 2–10 nm. The particle size distribution in the DI water solution is shown in Fig. 4c.

The zeta potential is an important property that characterizes the surface charge of particles or materials in a liquid medium. Carbon quantum dots (CQDs) are nanoscale carbon-based materials with unique properties, including high surface-to-volume ratio (S/V) and tunable surface chemistry. Fig. 4d presents the plot of the zeta potential study of PCQDs, which shows their better stability (−40 mV) and quantum-confined size.

Transmission microscopy allows us to visualize carbon quantum dots with high-resolution and three-dimensional imaging. It helps to characterize their size, shape, and distribution within a sample. Fig. 4a shows the TEM image at 50 nm scale, and Fig. 4b shows the enlarged aerial view of quantum dots. Confocal microscopy enables the imaging of these quantum dots to be observed based on their fluorescence emission, which provides their photophysical properties, such as emission wavelength, intensity, and lifetime.

Because of their unprecedented properties, quantum dots have potential for extraordinary applications in medication and drug pharmacy, particularly in cell labeling and long-term bio-imaging.[38] However, these nanoparticles cause reactive oxygen species to age, which has a negative impact on metabolic cycles and cell viability. The antioxidant potential of CQDs was determined *via* DPPH and H_2O_2 assays, as presented in Fig. S2.† CQDs and ascorbic acid were shown to have concentration-dependent DPPH radical-scavenging activity. The DPPH assessment uses the free-radical scavenging principle as its foundation. DPPH, or 1,1-diphenyl-2-picrylhydrazyl, is a purple, persistent free radical that absorbs light at 517 nm. When free radicals are scavenged, the colour of DPPH changes to yellow. Reactive oxygen species produce hydrogen peroxide (H_2O_2) as a metabolic byproduct. Antioxidant drugs can reduce H_2O_2 and regulate various oxidative stress-related states. CQDs at 20 μg mL^{-1} showed maximum radical-scavenging activity at around 48% during their H_2O_2 scavenging activity, and CQDs at 20 μg mL^{-1} showed total radical-scavenging activity of about 49% *via* their DPPH scavenging activity. As a result of these findings in the current investigation, the produced CQDs may be used as scavengers or inhibitors of free radicals. No significant (p = 0.05) changes were seen in any data for the parameters examined.

3.2 Optimization of formulation variables *via* complete factorial design

In this study, three independent variables, including albumin concentration, ethanol volume, and drug concentration, were considered, which significantly influenced the observed responses of particle size, zeta potential, and entrapment efficiency of resveratrol.

Particle size. The particle size range of the prepared albumin nanoparticle batches was found to be 118.3 to 177.8 nm. Run 8 showed the maximum particle size, while run 6 showed the minimum, as shown in Table 1.

Zeta potential. The zeta potential range of the prepared albumin nanoparticle batches was −6.65 to 0.104 mV. Table 1 displays the maximum and minimum PDI for runs 2 and 1, respectively.

Entrapment efficiency. The entrapment efficiency range of the prepared albumin nanoparticle batches was found to be 45.5

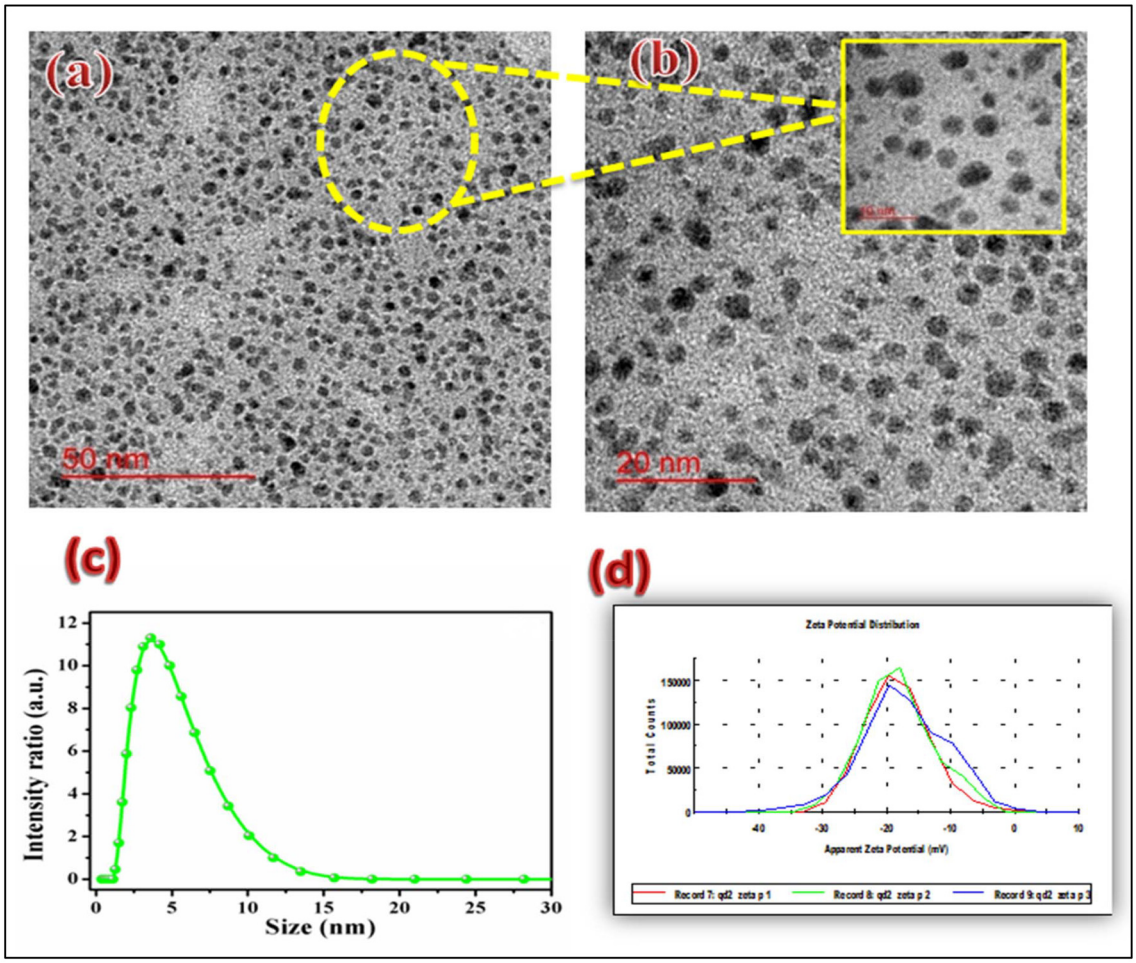

Fig. 4 (a) TEM image at the 50 nm scale, (b) TEM image at the 20 nm scale, (c) particle size distribution and (d) zeta potential study.

Table 1 Levels and factors for the design of the experiment (DOE)

Run	Albumin conc. (mg)	Ethanol (mL)	Resveratrol (mg)	Particle size (nm)	Zeta potential (mV)	Entrapment efficiency (%)
1	300	4	10	127.3	−6.65	75.2
2	200	12	10	129.4	0.104	53.3
3	250	8	7.5	155	−0.204	60.2
4	300	12	10	148	−4.04	45.5
5	200	4	10	126	−0.55	64.86
6	200	12	5	118.3	−0.103	46.4
7	300	12	5	125.6	−0.37	51.42
8	300	4	5	177.8	−0.44	59.87
9	200	4	5	145.4	−0.472	54.4

to 75.2%. The maximum entrapment efficiency was shown by run 1and the minimum by run 4, as shown in Table 1.

3.2.1 Effect of factors on particle size. For several combinations, the particle size ranged from 118.3 to 177.8 nm. The effects of factors such as albumin concentration, ethanol volume, and drug concentration on the particle size of albumin nanoparticles can be explained *via* response surface analysis curves. In a three-dimensional model, response surface analysis was demonstrated using the model polynomial function to show how vital independent factors affected the observed responses related to particle size. The surface response plot revealed that the particle size increases as the concentrations of albumin and drug increase.

3.2.2 Effect of factors on zeta potential. The zeta potential varied from −6.65 to 0.104 mV for various combinations. The effect of factors such as albumin concentration, ethanol volume, and drug concentration on the zeta potential of albumin nanoparticles can be explained by following response surface analysis curves. The response surface analysis was plotted using the model polynomial function in a three-dimen-

sional model to show how vital independent factors affected the zeta potential observed responses. The surface response plot revealed that the zeta potential decreases as albumin and drug concentrations decrease.

3.2.3 Effect of factors on entrapment efficiency. The entrapment efficiency varied from 45.5 to 75.2% for various combinations. The effect of variables like albumin concentration, ethanol volume, and drug concentration on the albumin nanoparticle entrapment efficiency can be identified by surface response curves. In a three-dimensional model, response surface analysis was shown using the model polynomial function to show that the significance of independent factors influences the observed responses of entrapment efficiency. The surface response plot revealed that as the drug concentration and ethanol volume decrease correspondingly, the entrapment efficiency increases.

3.2.4 Overlay plot for albumin nanoparticles. Fig. S4† exhibits the overlay plot, which depicts the prediction of an optimized formulation. This is represented by the area in the yellow region within which the exact criteria for the formula reside. Overlay plots are valuable tools in designing experiments to understand how various factors interact and influence the response variable.

3.3. Characterization of the optimized formulation

3.3.1 Particle size and zeta potential of the optimized formulation. The Zetasizer (NanoPlus-3, Japan) was utilized to measure the optimized average particle size of the formulation. It was discovered that the average particle size was 125.6 nm. The PDI of the optimized formulation was found to be 0.576. The polydispersity index measures the homogeneity. A homogeneous population is indicated by small PDI values ($\leq$0.1), whereas substantial heterogeneity is indicated by larger PDI values ($\geq$0.4). For stable formulations, the zeta potential usually lies in the range of −30 mV to +30 mV. The size of albumin nanoparticles can significantly influence the properties and performance of the formulation, including its drug release kinetics, bioavailability, and stability. In many applications, nanoparticles of this size are desirable as they often exhibit improved drug delivery characteristics, such as enhanced tissue penetration and reduced clearance by the immune system. The PDI value of 0.576 for the optimized formulation indicates some degree of particle size heterogeneity.[44] A PDI value above 0.4 suggests a relatively broad particle size distribution, indicating that not all nanoparticles are the same size. While a lower PDI is typically desired for a more homogeneous population, a PDI of 0.576 is not unusual for specific formulations. The zeta potential measures the electrokinetic potential at the surface of nanoparticles and is often used to indicate their stability. The zeta potential of the particles was recorded to be −0.570 mV, which can be considered stable as it is within the range of −30 mV to +30 mV. A greater charge would have indicated better stability.[34,40]

3.3.2 Surface morphology of the optimized formulation. The morphology of albumin nanoparticles was observed using SEM and TEM. Fig. S9(a)† shows an SEM image of albumin nanoparticles without the drug, while Fig. S9(b)† shows an SEM image of the optimized formulation in which spherical-shaped particles with sizes ranging between 81 and 200 nm may be visualized. Fig. S9(c)† shows the TEM image of the optimized albumin nanoparticles, where their size is 100 nm. The SEM images reveal the morphology of the albumin nanoparticles, providing information about their shape, size, and surface characteristics. In Fig. S9(a),† the SEM image of albumin nanoparticles without the drug shows the morphology of the nanoparticles when in their pristine state. The absence of drug molecules allows for a clear visualization of the morphology of the albumin nanoparticles. In Fig. S9(b),† the presence of the drug does not significantly alter the overall morphology of the nanoparticles, indicating that the drug is effectively incorporated within the albumin matrix without causing significant changes in particle size or shape. The TEM image confirms that the optimized albumin nanoparticles maintain a spherical shape, consistent with the observations from SEM imaging. The spherical morphology is desirable for drug delivery applications, as it promotes efficient cellular uptake, enhances circulation time, and controls drug release kinetics.

3.3.3 FTIR of the optimized formulation. The optimized formulation was scanned from a wavelength of 4000 cm^{-1} to 500 cm^{-1}. The resultant spectrum is shown in Fig. S10.† The IR spectrum of the optimized formulation reveals peaks recorded at 3280.1 cm^{-1} for the hydroxyl group (–OH), 1151.9 cm^{-1} for the alkyl amine, 696.7 cm^{-1} for the acid chlorides, 670.6 cm^{-1} for the carbonyl group and 1532.2 cm^{-1} for the aromatic ring. The identification of the hydroxyl group (–OH) suggests the presence of alcohol or phenolic compounds in the formulation, which may contribute to its solubility or intermolecular interactions. The detection of alkyl amine groups indicates the presence of organic amines, which may be used as stabilizers or surfactants in the formulation to enhance dispersion or prevent aggregation of nanoparticles. The identification of acid chlorides and carbonyl groups suggests the presence of carboxylic acid derivatives or esters, which may play a role in the formulation's chemical stability or drug release properties. The identification of aromatic rings indicates the presence of aromatic compounds, which may be part of the drug molecule or excipients used in the formulation.

3.3.4 XRD of the optimized formulation. The composition of the average bulk material is ascertained after the sample under analysis is homogenized and finely powdered. Solid powder samples were placed in a measurement holder for the XRD study. The samples were then scanned using the D8 Advance Eco X-ray diffractometer (Bruker, Germany). No peaks were observed because the drug was entrapped in the formulation. The absence of diffraction peaks in the obtained diffractogram indicates that the optimized formulation is amorphous and lacks a regular and repeating crystal structure. Instead, the atoms or molecules in the formulation are arranged in a disordered or random manner, resulting in diffuse scattering of X-rays. In the context of pharmaceutical

formulations or drug delivery systems, the amorphous nature of a formulation can have significant implications for its physical, chemical, and biological properties, including solubility, stability, dissolution rate, and bioavailability.

3.3.5 *In vitro* drug release. The *in vitro* release study of nine formulations and the optimized formulation in pH 7.4 buffer (normal cells) is shown in Fig. 5a. The maximum release of the drug was demonstrated in the pH 7.4 PBS, *i.e.*, 80% in 48 h. The chosen buffer closely mimics the body's physiological conditions where the drug is intended to act, and the drug release result indicates that the formulation can deliver the drug effectively in the desired environment. The variations in drug release profiles among the nine different formulations provide valuable insights into the impact of varying formulation parameters on drug release.[41] The release study in a pH 7.4 buffer is significant because it approximates the conditions in certain parts of the human body, such as the small intestine. Achieving high drug-release percentages within 48 hours indicates that the optimized formulation may suit drugs with specific dosing schedules or therapeutic needs. For instance, it could be well-suited for drugs that require sustained release over a defined period or for those targeting specific sites in the body.[41] The data indicate a difference in release profiles between pH 5 and pH 7.4, being more effective under acidic conditions. Since the pH in tumor microenvironments generally ranges from 5 to 7, the release was initially tested at a physiological pH of 7.4, assuming this would represent a baseline release rate. The release is anticipated to be enhanced in acidic pH, typical of cancer-affected areas. Consequently, as illustrated in Fig. 5b, it can be predicted that the nanoparticles will be stable and exhibit improved delivery efficacy in the acidic environment of tumors.

3.3.6 Release kinetics study. The release mechanism of resveratrol from the optimized formulation was ascertained by comparing their individual correlation coefficients (Fig. 6). The R^2 value for RSV release is highest in the Korsmeyer–Peppas model, *i.e.*, 0.935 and 0.9168 at pH 7.4 and 5. The Korsmeyer–Peppas model is the best fit for describing the release of resveratrol. This model is commonly used to describe drug release from polymeric systems and is often associated with non-Fickian (anomalous) release, indicating a combination of diffusion and polymer erosion-controlled release mechanisms. Utilizing the Korsmeyer–Peppas model to characterize the release of resveratrol from the optimized formulation offers a systematic approach to understanding drug release kinetics and optimizing drug delivery systems for *in vitro* cell-imaging applications, particularly in cancer research and therapy.

3.3.7 Antioxidant activity by DPPH assay and H_2O_2 assay. The antioxidant potential of albumin nanoparticle batches was determined *via* the DPPH and H_2O_2 assays, respectively. The DPPH test uses the free-radical scavenging principle as its base. DPPH, or 1,1-diphenyl-2-picrylhydrazyl, is a purple, persistent free radical that absorbs light at 517 nm. When free radicals are scavenged, DPPH changes to a yellow hue. The antioxidant treatment lowers (H_2O_2), a reactive oxygen metabolic by-product that is a crucial regulator for some oxidative stress-related conditions. Albumin nanoparticles exhibit over 90% scavenging activity in the DPPH and H_2O_2 assays, which strongly indicates their antioxidant potential. This high level of activity implies that these nanoparticles can neutralize or reduce the levels of harmful free radicals, such as DPPH and hydrogen peroxide, which can cause oxidative stress and damage to cells and tissues. The use of both DPPH and H_2O_2 assays is significant because it reflects the ability of the albumin nanoparticles to combat oxidative stress through different mechanisms.[42] DPPH is a stable free radical that is primarily tested for the ability to scavenge stable, non-reactive radicals, while H_2O_2 represents a more biologically relevant reactive oxygen species. The high scavenging activity in both assays suggests a broad spectrum of antioxidant action. Albumin nanoparticles can enhance the stability and bioavailability of antioxidants, making them more effective in therapeutic applications. These nanoparticles may offer advantages in drug delivery and controlled release of antioxidants.[43]

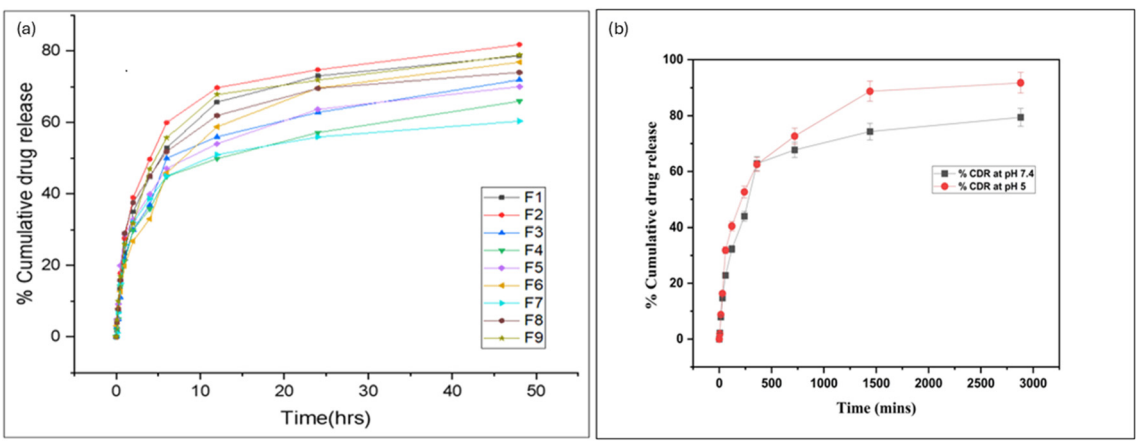

Fig. 5 *In vitro* drug release of (a) albumin nanoparticle batches F1–F9, (b) optimized formulation at pH 7.4 (physiological conditions) and pH 5 (acidic conditions).

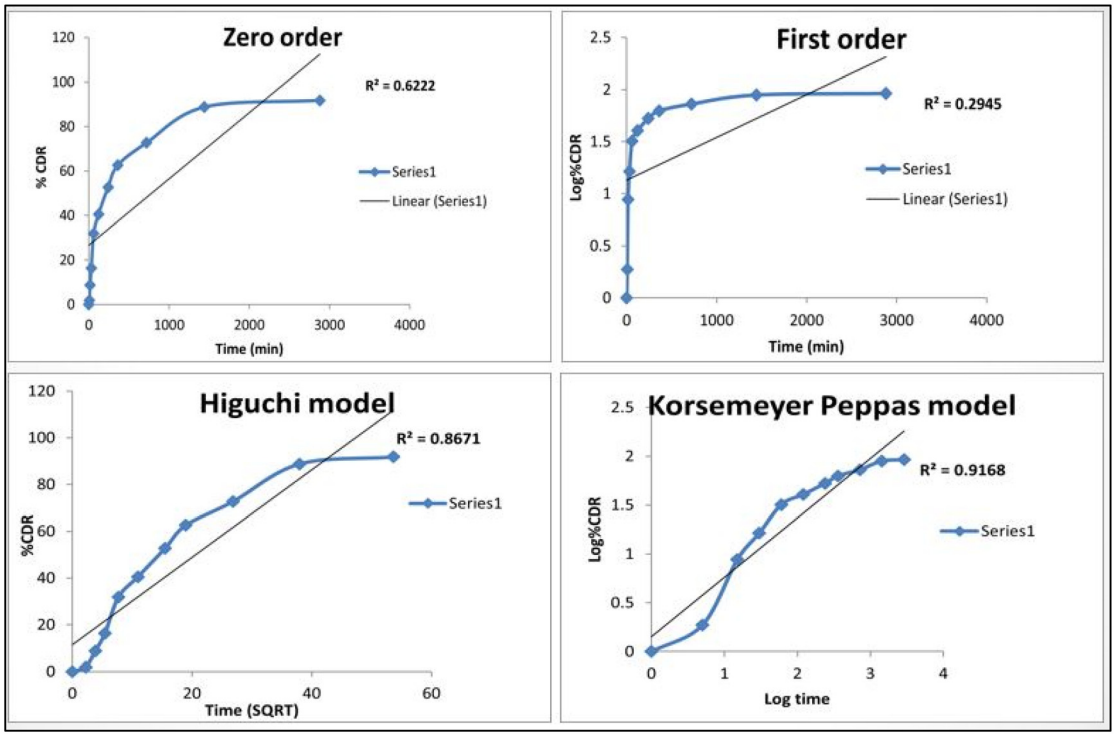

Fig. 6 *In vitro* drug release kinetics of the optimized formulation at pH 7.4 and pH 5.

The antioxidant potential of QDs, RSV, and the optimized formulation was also determined *via* the DPPH and H_2O_2 assays, respectively. DPPH, or 1,1-diphenyl-2-picrylhydrazyl, is a stable free radical with a purple color absorbed at 517 nm. When free radicals are scavenged, DPPH changes color to a yellow hue. Antioxidant activity of QDs was found to be 35–45%, and that of resveratrol was found to be 80–85% *via* both DPPH and H_2O_2. The optimized formulation has 96% antioxidant activity that shows a synergistic effect of QDs and RSV. The antioxidant activity of QDs, as assessed by both the DPPH and H_2O_2 assays, falls within the range of 35–45%. While this level of antioxidant activity is notable, it is relatively moderate compared to other antioxidant compounds. QDs are not typically known for their antioxidant properties, and their primary applications are often related to their unique optical and electronic properties. However, they may still have some capacity to scavenge free radicals to a certain extent. RSV exhibited higher antioxidant activity, ranging from 80–85% in the DPPH and H_2O_2 tests.[6] This is consistent with the known antioxidant potential of RSV, which has been extensively studied for its health benefits. The optimized formulation demonstrates 96% antioxidant activity in both assays. This result indicates a remarkable increase in antioxidant efficacy compared to the individual components (QDs and RSV). The synergistic impact shows that combining QDs and RSV in the optimized formulation has a substantially stronger antioxidant effect than the sum of their individual activities. (Fig. 7). Antioxidants play a crucial role in protecting cells and tissues from oxidative damage, and a formulation with a synergistic effect like this one may have significant benefits in combating oxidative stress-related conditions.[44]

3.3.8 Cytotoxicity assay of quantum dots

Mouse skin fibroblast cell line. According to Fig. 8, the % cell viability of L929 cells exposed to different concentrations of quantum dots was assessed by the MTT assay at 24, 48, 72, and 96 h. At each time, the values obtained for the control samples were taken as baseline values and compared with those of the corresponding exposed samples. The values are expressed as mean ± SEM of data from three separate studies. ($^*p < 0.05$, $^{**}p < 0.01$, $^{***}p < 0.001$, $^{****}p < 0.0001$). The percentage cell viability at 24 h for all the concentrations reduced significantly compared to the control, except for the 0.25 mg mL^{-1} concentration that did not affect cells. Approximately 90% of cells were viable at 1 mg mL^{-1} concentration up to 24 h of exposure, and more than 90% were viable at 2 mg mL^{-1} concentration up to 24 h. However, beyond 24 hours, the quantum dots might have degraded in the medium, allowing the cells to restore their normal physiological function. This is reflected by the increase in the percentage cell viability up to 96 h.[45] Based on the results of the cell viability study, it was observed that increasing the quantum dot sample concentration did not significantly affect normal cells. This is likely due to the use of natural paddy husk in synthesizing the quantum dots. Therefore, we can predict that the quantum dots are safe for normal cells.

Metastatic breast cancer cell line. After treating MDA-MB-231 cells with QDs for 24 h, MTT assays were performed to esti-

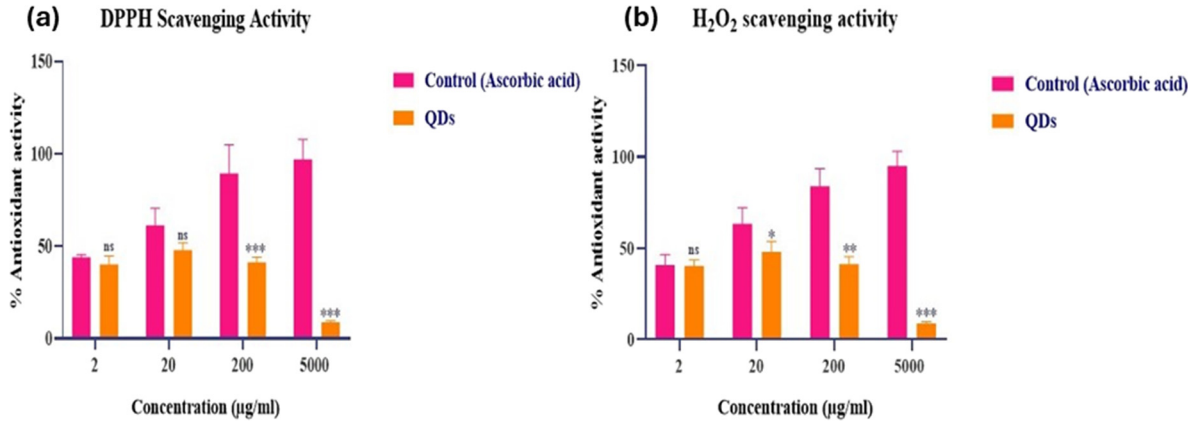

Fig. 7 (a) DPPH assay graph of QDs, RSV, and optimized formulation and (b) H_2O_2 antioxidant assay graph of QDs, RSV, and optimized formulation. Mean ± SD (n = 3) [n.s. (not significant) * <0.05, ** <0.01, *** <0.001, **** <0.0001] significant difference in comparison with control.

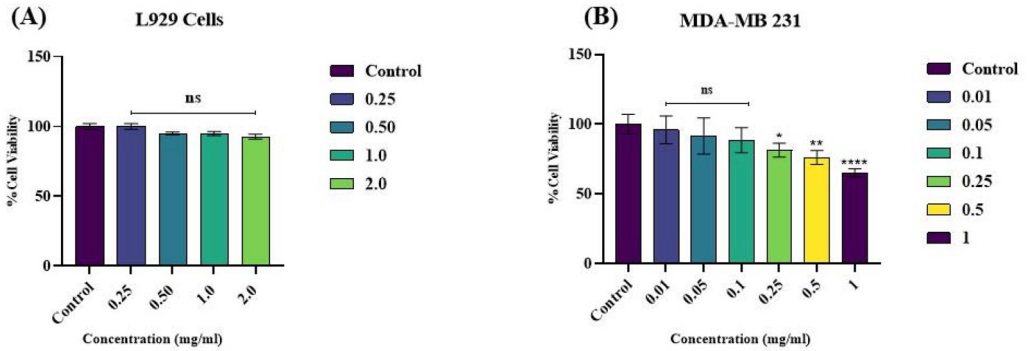

Fig. 8 (A) Percentage cell viability at different concentrations of these treatments for 24 h on L929 cells. Mean ± SD (n = 3) [n.s. (not significant) * <0.05, ** <0.01, *** <0.001, **** <0.0001] significant difference in comparison with control. (B) Percentage cell viability at different concentrations of these treatments for 24 h on MDA-MB-231 cells. Mean ± SD (n = 4) [n.s. (not significant) * <0.05, ** <0.01, *** <0.001, **** <0.0001] significant difference in comparison with control.

mate the cytotoxicity of the QDs on malignant cells. When the applied QD concentrations ranged from 1 to 1000 µg mL^{-1} for MDA-MB-231 cells treated for 24 h, the cell viability of the three groups was maintained at over 90%. For L929 cells treated for 24 h, the trends in cell viability followed a similar pattern; the cell viability was maintained at over 80% for 0.1 mg mL^{-1}. However, a different pattern was observed when we increased the incubation period to 48 h. As the QD concentration rose 48 h after treatment, cell viability dropped, indicating that the QDs had concentration-dependent cytotoxicity on cell viability. Cancerous cells have a cell membrane that is leaky or ruptured. Due to this, quantum dots can easily cross the cell membrane and cause cytotoxicity, or cell death, to cancer cells. If the quantum dots are loaded with an anticancer drug within a suitable carrier, it could be a better drug delivery method for cancer treatment.

Cytotoxicity assay for albumin nanoparticles. The cytotoxicity of the samples (RSV, QD, and optimized albumin nanoparticles) was evaluated by the MTT assay on MDA-MB-231 cells. The results of the MTT assay revealed the compatibility of the QDs. QDs showed 64.93 ± 3.12% cell viability at the higher concentration of 1000 µg mL^{-1}, RSV showed 41.71 ± 6.98% cell viability at the concentration of 1000 µg mL^{-1}, and for the optimized formulation it was found to be 15.76 ± 1.76%. IC_{50} values for RSV, QDs, and optimized albumin nanoparticles were 104.4 µg mL^{-1}, 1551 µg mL^{-1}, and 51 µg mL^{-1}, respectively. The IC_{50} value of the optimized formulation is low because the drug accumulation in the cells is higher than the naïve drug and quantum dots. However, loading this drug and quantum dots into a carrier like albumin nanoparticles shows a better cytotoxicity effect on cancerous cell lines. Due to the nano-size range of particles and better internalization into cells, the lowest IC_{50} concentration was found in the final optimized nanoformulations.

Fig. 9 shows morphological evaluations of MDA-MB-231 cells after treatment with RSV, QDs, and the optimized formulation. Quantum dots have very high cell viability, meaning they are nontoxic because they are synthesized from a natural

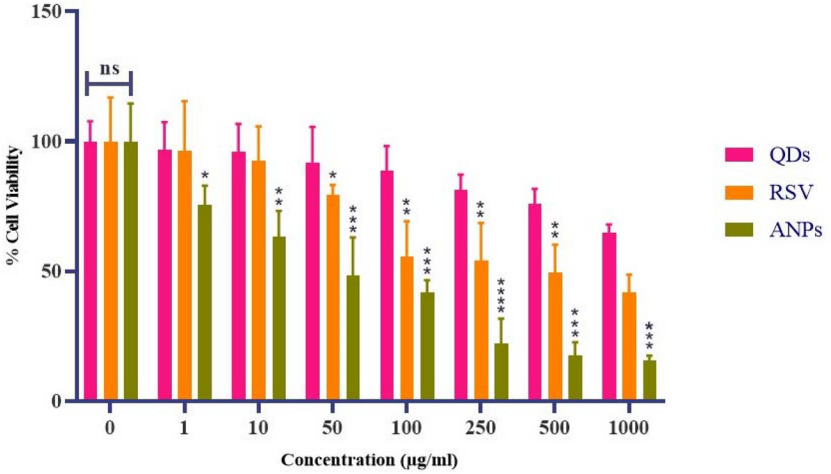

Fig. 9 Percentage cell viability of QDs, RSV, and the optimized formulation (ANPs).

source. Cell-to-cell adhesion was lost in the RSV and optimized formulation, leading to cell blebbing conditions.[46] One of the components of human blood is albumin. As an endogenous protein (35–50 g L^{-1} human serum), it exhibits minimal immunogenicity, and albumin-based nanoparticles guarantee its biocompatibility. In human blood, albumin has an average half-life of about 19 days. Albumin has a longer half-life than free medicines, which helps increase the plasma area under the curve (AUC) value and sustain a high plasma drug concentration for a considerable time.

3.3.9 ***In vitro* cell imaging.** The potential use of QDs for live-cell imaging was confirmed by using QDs as probes during laser scanning confocal microscope imaging with MDA-MB-231 cells. The fluorescence signal of the QDs appeared mainly in the cytoplasm, indicating that the QDs could be used for *in vitro* breast cancer cell bioimaging. The optimized formulation (albumin nanoparticles) shows better cellular internalization than QDs. The optimized formulation increases circulation time as it may circumvent RES uptake as the particle becomes more extensive and improves half-life. Prolonged circulation time allows nanoparticles to accumulate preferentially in tumour tissues *via* the enhanced permeability and retention (EPR) effect, thereby improving the efficacy and specificity of cancer therapy while minimizing off-target

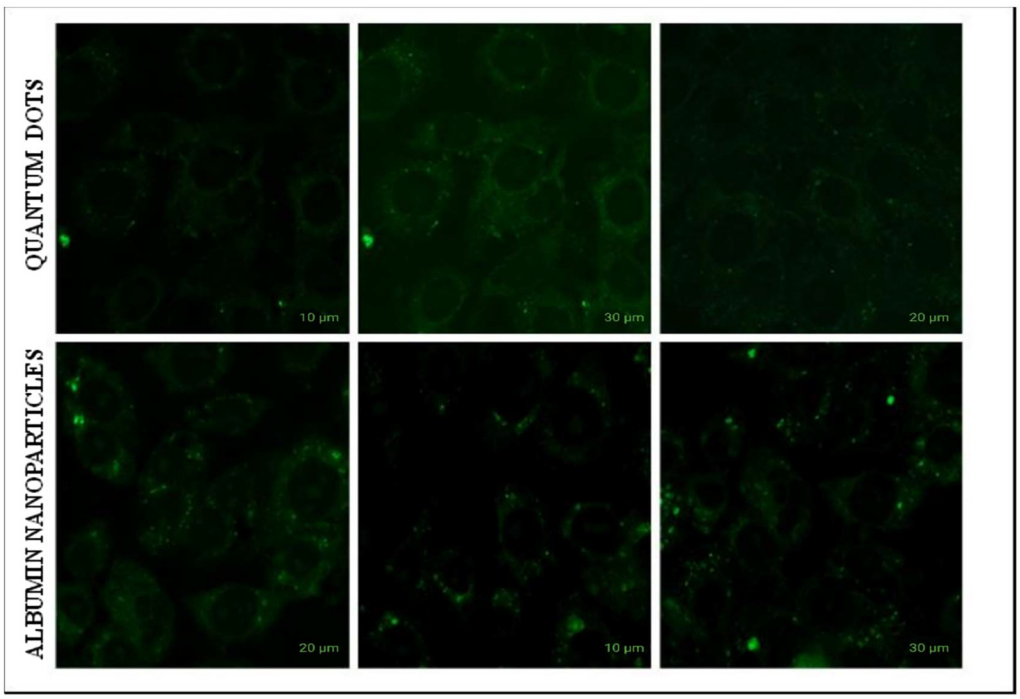

Fig. 10 *In vitro* cell imaging of MDA-MB-231 cells after treatment with QDs and optimized formulation.

effects. Moreover, the surface functionalization of nanoparticles with targeting ligands, such as antibodies or peptides, can further enhance their tumour-targeting capabilities, enabling precise delivery of therapeutic payloads to breast cancer cells while sparing healthy tissues (Fig. 10). The ability to visualize and quantify cellular events in real-time using QDs can facilitate the discovery of novel biomarkers and therapeutic targets for breast cancer diagnosis and treatment.

4. Conclusion

QDs lead to many unique optical and transport properties. They are environmentally safe, easily handled, non-toxic, and can be made from a high-carbon source. The current project focuses on synthesizing quantum dots from an agricultural material (paddy husk) employed for fluorescence and bioimaging features. Resveratrol, a powerful antioxidant, has limitations, such as low solubility, short half-life (<1 h), and low circulation time. Delivering the resveratrol *via* a suitable nanocarrier and utilizing QDs for their synergistic antioxidant activity was achieved. Combining resveratrol and quantum dots in albumin nanoparticles enhanced the antioxidant activity. The prepared nanoparticles had multifunctional properties (synergized antioxidant efficacy, delivery, and bioimaging). The current study successfully utilized QDs as probes for imaging in MDA-MB-231 cells. Results obtained were satisfactory, with superior imaging and enhanced antioxidant activity, suggesting that the work undertaken has good translational potential. The study can be conducted with other drugs for potential applications in theranostics as future scope.

Conflicts of interest

The authors declare that there is no conflict of interest.

References

1 M. A. Mahjoub, G. Monier, C. Robert-Goumet, F. Réveret, M. Echabaane, D. Chaudanson, M. Petit, L. Bideux and B. Gruzza, *J. Phys. Chem. C*, 2016, **120**, 11652–11662.
2 M. Kurian and A. Paul, *Carbon Trends*, 2021, **3**, 100032.
3 M. Ballabio and E. Cánovas, *ACS Nanosci. Au*, 2022, **2**, 367–395.
4 L. Llatance-Guevara, N. E. Flores, G. O. Barrionuevo and J. L. Mullo Casillas, *Catalysts*, 2022, **12**, 1091.
5 N. A. A. Nazri, N. H. Azeman, M. H. A. Bakar, N. N. Mobarak, T. H. T. A. Aziz, A. R. M. Zain, N. Arsad, Y. Luo and A. A. A. Bakar, *Nanomaterials*, 2022, **12**, 2999.
6 R. Das, R. Bandyopadhyay and P. Pramanik, *Mater. Today Chem.*, 2018, **8**, 96–109.
7 K. J. Nordell, E. M. Boatman and G. C. Lisensky, *J. Chem. Educ.*, 2005, **82**, 1697.
8 M. Hamer, E. Tóvári, M. Zhu, M. D. Thompson, A. Mayorov, J. Prance, Y. Lee, R. P. Haley, Z. R. Kudrynskyi, A. Patanè, D. Terry, Z. D. Kovalyuk, K. Ensslin, A. V. Kretinin, A. Geim and R. Gorbachev, *Nano Lett.*, 2018, **18**, 3950–3955.
9 W. Widowati, C. N. Ginting, I. N. E. Lister, E. Girsang, A. Amalia, S. H. B. Wibowo, H. Kusuma and Rizal, *Trop. Life Sci. Res.*, 2020, **31**, 127–144.
10 J. Zhou, Z. Sheng, H. Han, M. Zou and C. Li, *Mater. Lett.*, 2012, **66**, 222–224.
11 A. Nair, J. T. Haponiuk, S. Thomas and S. Gopi, *Biomed. Pharmacother.*, 2020, **132**, 110834.
12 R. K. Shukla, V. Sharma, A. K. Pandey, S. Singh, S. Sultana and A. Dhawan, *Toxicol. in Vitro*, 2011, **25**, 231–241.
13 V. Singh, T. Marimuthu, M. M. Makatini and Y. E. Choonara, *Polymers*, 2022, **14**, 5371.
14 E. Atta, N. Mohamed and A. Abdelgawad, *Eur. Chem. Bull.*, 2017, **6**, 365–375.
15 A. Srivastava, S. Singh, A. Pandey, D. Kumar, C. Rajpurohit, V. Khanna and A. Pant, *Mol. Neurobiol.*, 2018, **55**, 8293–8305.
16 A. Sharma, P. Chaudhary, A. Verma, R. K. Tripathi, R. Kumar, G. Gupta, D. P. Mondal, B. C. Yadav and A. K. Srivastava, *ECS J. Solid State Sci. Technol.*, 2023, **12**, 27004.
17 Z. Zhang, W. Sun and P. Wu, *ACS Sustainable Chem. Eng.*, 2015, **3**, 1412–1418.
18 A. Zarepour, A. Khosravi, N. Yücel Ayten, P. Çakır Hatır, S. Iravani and A. Zarrabi, *J. Mater. Chem. B*, 2024, **12**, 4307–4334.
19 A. Nair, J. T. Haponiuk, S. Thomas and S. Gopi, *Biomed. Pharmacother.*, 2020, **132**, 110834.
20 N. S. Kulkarni, Y. Guererro, N. Gupta, A. Muth and V. Gupta, *J. Drug Delivery Sci. Technol.*, 2019, **49**, 352–364.
21 S. Wang, L. Chen, J. Wang, J. Du, Q. Li, Y. Gao, S. Yu and Y. Yang, *Mater. Sci. Eng., C*, 2020, **116**, 111233.
22 E. Dhandapani, N. Duraisamy and R. Mohan Raj, *Mater. Today: Proc.*, 2022, **51**, 1696–1700.
23 F. F. An and X. H. Zhang, *Theranostics*, 2017, **7**, 3667–3689.
24 Y. Hangun-Balkir and M. L. McKenney, *Green Chem. Lett. Rev.*, 2012, **5**, 147–153.
25 X. Liu, G. B. Braun, H. Zhong, D. J. Hall, W. Han, M. Qin, C. Zhao, M. Wang, Z. G. She, C. Cao, M. J. Sailor, W. B. Stallcup, E. Ruoslahti and K. N. Sugahara, *Adv. Funct. Mater.*, 2016, **26**, 267–276.
26 N. Lomis, S. Westfall, L. Farahdel, M. Malhotra, D. Shum-Tim and S. Prakash, *Nanomaterials*, 2016, **6**, 116.
27 I. Gülçin, *Innovative Food Sci. Emerging Technol.*, 2010, **11**, 210–218.
28 B. D. Mansuriya and Z. Altintas, *Materials*, 2020, **13**, 96.
29 L. Zhao, Y. Wang and Y. Li, *Nanomaterials*, 2019, **9**, 1708.
30 F. F. An and X. H. Zhang, *Theranostics*, 2017, **7**, 3667–3689.
31 S. Chakraborty, I. Ehsan, B. Mukherjee, L. Mondal, S. Roy, K. Das Saha, B. Paul, M. C. Debnath and T. Bera, *Nanomedicine*, 2019, **20**, 102006.

32 A. Al Hoque, D. Dutta, B. Paul, L. Kumari, I. Ehsan, M. Dhara, B. Mukherjee, M. Quadir, B. A. Kaipparettu, S. Laha and S. Ganguly, *Cancer Nanotechnol.*, 2023, **14**, 73.
33 I. Ehsan, L. Kumari, R. Sen, A. Hoque, B. Mukherjee, A. Mukherjee, P. Ghosh and S. Bhattacharya, *J. Drug Delivery Sci. Technol.*, 2022, **75**, 103689.
34 M. M. M. Zayed, H. A. Sahyon, N. A. N. Hanafy and M. A. El-Kemary, *Pharmaceutics*, 2022, **14**, 1160.
35 L. Zhao, Y. Wang and Y. Li, *Nanomaterials*, 2019, **9**, 1708.
36 C. E. Bradburne, J. B. Delehanty, K. Boeneman Gemmill, B. C. Mei, H. Mattoussi, K. Susumu, J. B. Blanco-Canosa, P. E. Dawson and I. L. Medintz, *Bioconjugate Chem.*, 2013, **24**, 1570–1583.
37 Z. Liang, M. B. Khawar, J. Liang and H. Sun, *Front. Oncol.*, 2021, **11**, 749970.
38 K. D. Wegner and N. Hildebrandt, *Chem. Soc. Rev.*, 2015, **44**, 4792–4834.
39 A. Foerster and N. A. Besley, *J. Phys. Chem. A*, 2022, **126**, 2899–2908.
40 J. Drbohlavova, V. Adam, R. Kizek and J. Hubalek, *Int. J. Mol. Sci.*, 2009, **10**, 656–673.
41 J. M. Llabot, I. Luis de Redin, M. Agüeros, M. J. Dávila Caballero, C. Boiero, J. M. Irache and D. Allemandi, *J. Drug Delivery Sci. Technol.*, 2019, **52**, 379–385.
42 A. Jithan, K. Madhavi, M. Madhavi and K. Prabhakar, *Int. J. Pharm. Invest.*, 2011, **1**, 119.
43 V. Lobo, A. Patil, A. Phatak and N. Chandra, *Pharmacogn. Rev.*, 2010, **4**, 118–126.
44 P. Yadav and A. Yadav, *Futur. J. Pharm. Sci.*, 2021, **7**, 200.
45 R. A. , S. Jagadeesan, Y.-J. Cho, J.-H. Lim and K. H. Choi, *Mater. Sci. Eng., C*, 2017, **81**, 551–560.
46 A. Sabzi, A. Rahmani, M. Edalati, H. Kahroba, M. R. Dadpour, R. Salehi and A. Zarebkohan, *Colloids Surf., B*, 2020, **194**, 111225.